Ultramicroscopy 160 (2016) 118–129

Contents lists available at ScienceDirect

Ultramicroscopy

journal homepage: www.elsevier.com/locate/ultramic

A novel 3D absorption correction method for quantitative EDX-STEM tomography

Pierre Burdet [a,*], Z. Saghi [a], A.N. Filippin [b], A. Borrás [b], P.A. Midgley [a]

[a] Department of Materials Science and Metallurgy, University of Cambridge, Charles Babbage Road 27, Cambridge CB3 0FS, Cambridgeshire, UK
[b] Nanotechnology on Surfaces Laboratory, Materials Science Institute of Seville (ICMS), CSIC-University of Seville, C/ Americo Vespucio 49, 41092 Seville, Spain

ARTICLE INFO

Article history:
Received 1 April 2015
Received in revised form
18 September 2015
Accepted 26 September 2015
Available online 3 October 2015

Keywords:
Energy dispersive X-ray spectrometry
Electron tomography
3D chemical analysis
Quantification
Absorption correction

ABSTRACT

This paper presents a novel 3D method to correct for absorption in energy dispersive X-ray (EDX) microanalysis of heterogeneous samples of unknown structure and composition. By using STEM-based tomography coupled with EDX, an initial 3D reconstruction is used to extract the location of generated X-rays as well as the X-ray path through the sample to the surface. The absorption correction needed to retrieve the generated X-ray intensity is then calculated voxel-by-voxel estimating the different compositions encountered by the X-ray. The method is applied to a core/shell nanowire containing carbon and oxygen, two elements generating highly absorbed low energy X-rays. Absorption is shown to cause major reconstruction artefacts, in the form of an incomplete recovery of the oxide and an erroneous presence of carbon in the shell. By applying the correction method, these artefacts are greatly reduced. The accuracy of the method is assessed using reference X-ray lines with low absorption.

1. Introduction

EDX microanalysis in the transmission electron microscope (TEM) is a valuable technique for materials characterisation [1–4]. Until recently, the technique has been limited by poor collection efficiency, and hence relatively long acquisition times [4,5]. With the advent of larger, silicon drift [6] and multiple detectors [7], modern systems offer higher acquisition rates for a lower dose. EDX chemical mapping has benefited greatly from this technological breakthrough, especially in helping the extension to (quantitative) 3D mapping, as observed recently with a wider range of applications [8–15] compared to the early work of the pioneers [16–18].

In a scanning transmission electron microscope (STEM), 2D imaging can be extended to three-dimensional (3D) imaging by using tomography. Electron tomography (ET) is nowadays a well-established technique in the physical sciences, especially using high angle annular dark field (HAADF) imaging [19–21]. To be suitable for tomographic reconstruction, the electron–specimen interaction should satisfy the "projection requirement": the signal should vary at least monotonically with thickness and composition [22]. When detecting secondary signals, such as X-rays for EDX, the interaction with the specimen needs to be considered as well. To illustrate the interactions of primary electrons and secondary X-rays with the specimen, two electron paths through a core/shell nanowire are considered (see the arrows in Fig. 1). The generated X-ray intensities along these symmetric paths are identical. However, as the path towards the EDX detector for the right-hand position is longer (and goes through the core), X-rays are more likely to be absorbed in the specimen, yielding a lower X-ray intensity. Variations either due to absorption or changes in specimen composition may be indistinguishable when absorption is significant, as will be true for low energy X-rays and/or thick samples. This paper aims to correct for the absorption effect in order to retrieve a monotonic behaviour for the EDX signal and improve the reliability of the 3D EDX-STEM reconstructions. It is worth noting that other phenomena, beyond the scope of the current work, might also break the monotonicity of the EDX signal, such as channelling effects [23] and detector shadowing by the sample holder and the sample grid [13].

X-ray absorption is one of the most important limitations for quantitative EDX analysis, even with thin specimens. Goldstein et al. [24] proposed a corrections for absorption using the Cliff–Lorimer approach (CL) [25] by multiplying the X-ray intensity by a correction factor (A). This factor is derived from Beer's law and requires a measurement of the mass-thickness. To overcome the complications arising from external measurement of thickness and density, several approaches have been proposed: for instance by using the difference in absorption between two emitted X-ray lines [26], or measuring spectra at different tilt angles [27] or sample thicknesses [28]. A more recent approach, the ζ-factor method [29], solved this problem in a more general way by

* Corresponding author. Fax: +44 1223 334563.
E-mail address: pierre.burdet@a3.epfl.ch (P. Burdet).

http://dx.doi.org/10.1016/j.ultramic.2015.09.012

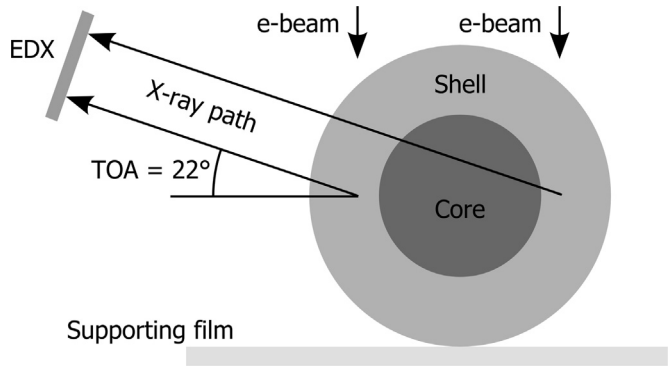

Fig. 1. X-ray absorption in a core/shell nanowire. The X-rays are generated in a nanowire supported by a film. The arrows show two X-ray paths through the sample towards an EDX detector. A typical elevation angle is given.

measuring the current. All these approaches were established for thin films and aim to measure an accurate absorption correction factor *A*, supposing a homogeneous specimen where X-rays are generated and absorbed. To apply this approach to a sample with a heterogeneous structure, such as the core/shell nanowire of Fig. 1, the structure has to be known to predict the X-ray generation as a function of depth as well as the X-ray path to the surface through different materials. This problem can be addressed with 3D EDX-STEM tomography since information about X-rays generated from each voxel and their path through all the encountered voxels to reach the surface becomes available.

The present work introduces a novel "3D absorption correction" approach. An example of EDX-STEM tomography with greatly reduced artefacts is presented, using a core/shell nanowire as test sample. The accuracy of the absorption correction method is assessed using X-ray lines with significant absorption and high energy X-ray lines with relatively low absorption as a reference.

2. Materials and methods

2.1. Core/multi-shell nanowire

The sample used for the present investigation is an organic/inorganic core/multi-shell 1-D nanostructure, with potential applications in photonics [30] and as nanogenerators [31]. A HAADF-STEM image of the nanowire (NW) tip is shown in Fig. 2(a) and a description of the different elements present in the sample is schematized in Fig. 2(b). The metal-organic compound platinum octaethylporphyrin (PtOEP) forms the core. It is grown from silver nanoparticle seeds by physical vapour deposition, is composed primarily of platinum, nitrogen and carbon. The first shell of the 1-D nanodevice is generated by soft plasma etching of the PtOEP to yield platinum [32]. An unexpected AgPt phase is also present as particles in the core and as a thin layer around the core. The second shell is formed of ZnO grown by plasma enhanced chemical vapour deposition [30]. The external shell is fabricated by conformal deposition of a thin layer of gold by means of DC sputtering at room temperature.

2.2. EDX-STEM tomography

The ET experiment was performed on an FEI Osiris TEM (FEI company) operating at 200 kV and equipped with a high brightness X-FEG gun and a Super-X EDX system comprising four detectors. Each detector has an active area of 30 mm^2, achieving 0.9 sr solid angle in total. As shown in Fig. 3, the four detectors are arranged around the electron beam axis. The elevation angle (for the centre of each detector) is 22° and the azimuth angles are 45°, 135°, 225° and 315° for detector 1, 4, 3 and 2, respectively. The signals from the different detectors are summed before amplification and cannot be separated through post-processing. The NWs were dispersed on a commercial TEM grid possessing a 5 nm-thick carbon film on a thicker 30 nm holey carbon film (Pacific Grid Tech), which was mounted on a Fischione 2020 single-tilt tomography holder (Fischione Instruments, USA). A NW oriented parallel to the rotation axis was selected, and the tilt series was acquired manually, from $-60°$ to $+70°$ with a 10° tilt increment. At each tilt angle, a HAADF-STEM image with frame size of 1024×1024 and a pixel size of 1.09 nm was acquired, followed by an EDX map of a selected region, with a map size of 80×92 pixels and a pixel size of 4.5 nm. The beam current was 600 pA. To reduce beam damage, a short dwell time of 40 ms was used, corresponding to an acquisition time of 5 min per map. Depending on the acquisition geometry, some of the X-rays emitted from the

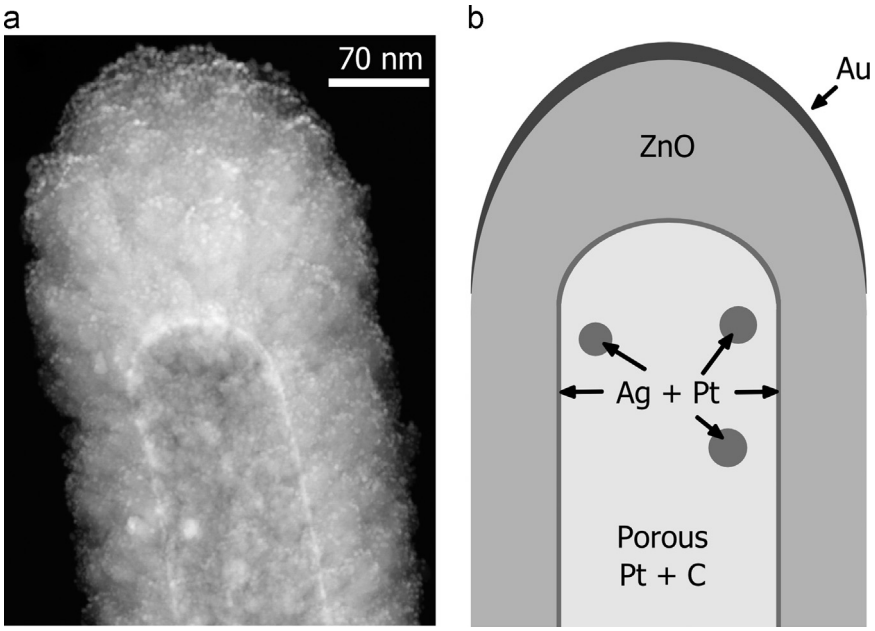

Fig. 2. Tip of a core/shell nanowire. (a) High angular annular dark field (HAADF) micrograph. (b) Schematic cross-section of the sample. The different phases are indicated.

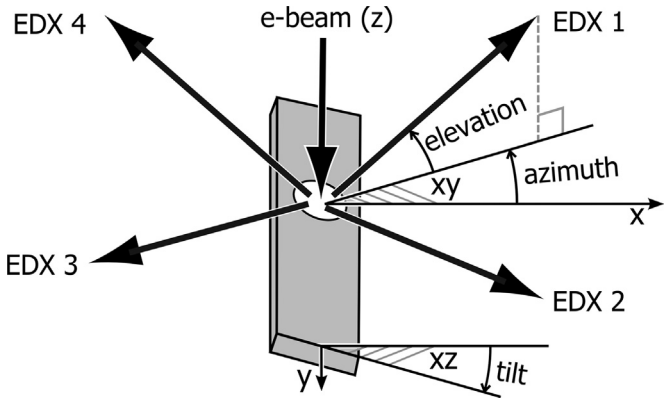

Fig. 3. Geometry for 3D EDX-STEM acquisition. The grey box represents the sample holder. The electron beam direction is vertical and defines the *z* axis. The elevation angle is the take-off angle for an untilted surface. The azimuth is the angle between the *x* axis and the projection of the detector direction on an untilted surface. The *y* axis is the rotation axis of the tilt.

region of interest are obstructed by surrounding objects such as the sample holder and supporting grid. As the elevation angle is low, the shadow cast onto the detectors varies rapidly with tilt angle around 0°. To minimise the effect of shadowing, only the two detectors facing the sample were used during the tilt series; i.e. detector 1 and 2 for positive tilt (including 0° tilt) and detector 3 and 4 for negative tilt.

The sum of all spectra of the tilt series is plotted in Fig. 4 with a solid curve. The energy range between 3.5 and 7 keV is not displayed, as it contains no X-ray lines of importance. X-ray lines for the six elements that composed the core/shell nanowire (C, O, Zn, Pt, Au and Ag) are observed. Carbon and oxygen have only one resolved line, the O Kα and C Kα, respectively, which have the lowest energy of the analysed X-ray lines. Cu Kα and Ni Kα peaks are spurious X-rays generated from the supporting nickel grid and the sample holder. The Si Kα and Cl Kα signals are likely due to contamination from volatile organosilicon compounds used in the desiccator where the silver seeds were stored.

Also in Fig. 4, the mass absorption coefficients μ/ρ of X-rays absorbed in PtC_{25} and ZnO, two compositions chosen to approximate the nanowire core and shell respectively, are plotted as a function of energy with dashed curves. The jumps in the curves are the X-ray absorption edges, corresponding to the ionisation energy of inner shell electrons. These edges are situated at slightly

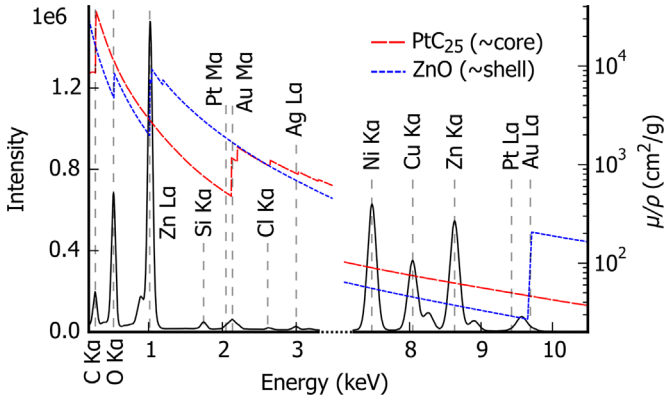

Fig. 4. X-ray lines emitted from a core/shell nanowire and corresponding absorption coefficients. The EDX spectrum, a sum over all spectra of the tilt series, is plotted with a solid black curve (left scale). The mass absorption coefficients μ/ρ of X-rays absorbed in PtC_{25} and ZnO, composition approximating the core and the shell respectively, are plotted as a function of energy with dashed curves (right scale). The centre of the main X-ray peaks are indicated by vertical dashed lines. Minor lines are not labelled.

higher energy than the corresponding X-ray lines; for instance the centre of Zn Lα peak is slightly left of the corresponding jump on the blue curve. Zn Kα and Pt Lα have a μ/ρ about two orders of magnitude lower than the three most highly absorbed X-rays (C Kα, O Kα, Zn Lα), making the Zn Kα intensity a suitable internal reference, with low absorption compared to the Zn Lα intensity.

The EDX maps were acquired using the software TIA (FEI company) and exported for post-processing. Apart from alignment, all data processing was done with python packages. Hyperspy, a python-based software for hyperspectral data processing [33], was used as a central data processing platform and to implement the absorption correction procedure. The data were denoised using singular value decomposition (SVD) for principal component analysis (PCA) [34]. X-ray intensities were extracted from EDX spectra by fitting (peaks and background) experimental spectra using an EDX-specific model [35]. TomoJ was then used for alignment by automatic feature tracking [36]. The reconstructions were performed using the simultaneous algebraic reconstruction technique (SART) algorithm [37], and the obtained volumes rendered using Mayavi [38]. Elemental compositions were quantified using the CL quantification method [25] and the *k*-factors provided by the EDX manufacturer Bruker. A total variation minimisation (TV) algorithm from Chambolle [39] was used to improve the signal-to-noise ratio in the obtained reconstructions. One iteration of the absorption correction, including the reconstruction of all X-ray intensities, takes about 24 min on a standard computer (one processor of 3.4 GHz). The slower parts of the process were parallelised and the time per iteration was reduced to 6 minutes with 8 processors.

3. Calculation

In the classical CL approach, the composition C is related to the X-ray intensities I measured from a thin film [25]. With two elements A and B, the CL approach can correct for the absorption using [24]:

$$\frac{C_A}{C_B}=k_{AB}\frac{I_A A_A}{I_B A_B} \tag{1}$$

where k is the CL factor, also known as the *k*-factor, and A is the absorption correction factor related to the X-ray lines. In the typical expression for CL, a singular absorption correction factor A_{AB} is given for the intensity ratio between elements ($A_{AB}=A_A/A_B$). The more recent ζ-factor method incorporates the total dose during acquisition D_e, obtaining in this way a measurement of the composition and the mass-thickness ρt as:

$$C_A=\frac{\zeta_A I_A A_A}{\zeta_A I_A A_A+\zeta_B I_B A_B} \tag{2a}$$

$$\rho t=\frac{\zeta_A I_A A_A+\zeta_B I_B A_B}{D_e} \tag{2b}$$

where ζ is the ζ-factor [40]. Both *k*-factors and ζ-factors can be determined theoretically and experimentally.

The A factors for both the CL and ζ-factor methods are derived from Beer's law, which predicts the X-ray absorption in a material. The X-ray intensity I emerging from a thin film of thickness t is: $I = I_0 \exp\left(-\frac{\mu}{\rho}\rho t\right)$, where I_o is the primary X-ray intensity, μ/ρ is the mass absorption coefficient and ρ is the density. With $\varphi(\rho z)$ the depth distribution of the generated X-rays in the sample, and assuming a homogeneous X-ray absorption along the path z to the surface, the absorption correction factor A is obtained by integrating Beer's law as follow:

$$A=\frac{I_0}{I}=\frac{\int_0^{\rho t}\varphi(\rho z)d(\rho z)}{\int_0^{\rho t}\varphi(\rho z)\exp\left(-\frac{\mu}{\rho}\rho z\csc\alpha\right)d(\rho z)} \quad (3)$$

where α is the take-off angle and $z\csc\alpha$ is equal to the distance from the generation point to the surface. For high energy electrons, a uniform generation of X-rays along the depth can be reasonably assumed within a thin film: $\varphi(\rho z)$ is then equal to one and Eq. (3) is simplified to (Philibert [41]):

$$A=\frac{\frac{\mu}{\rho}\rho z\csc\alpha}{1-\exp\left(-\frac{\mu}{\rho}\rho z\csc\alpha\right)} \quad (4)$$

This expression for A is used in both the CL and ζ-factor methods [24,40].

Correcting the absorption in 3D allows us to refine the approximation of a constant generation and of a homogeneous X-ray path by considering the X-ray generation in each voxel and the different voxels encountered in the X-ray path to the surface. The X-ray generation is thus assumed to be constant in each voxel and the X-ray path is assumed to be homogeneous within each voxel encountered.

In Fig. 5(a), a section through the x–z plane of the 3D matrix of elemental composition $\mathbf{C}$ is represented with a grid. A precipitate is represented with a darker grey than a surrounding matrix. The X-ray path, represented by the arrow, has a different length in each encountered voxel. In a standard reference frame, the z axis is parallel to the electron beam as shown in Fig. 5(a). In Fig. 5(b), a new reference frame x^*, y^* and z^* is defined with x^* axis parallel to the detector direction. The composition matrix in this reference frame ($\mathbf{C}^*$) is obtained by rotating $\mathbf{C}$ by the elevation angle, the sample tilt and the azimuth angle of the detector. In each encountered voxel of the matrix $\mathbf{C}^*$, the X-ray path has the same length (the voxel size Δx), thus simplifying the calculation of the absorption correction factor A_j^* of voxel $x^*=j$.

An X-ray intensity I_0 is generated in voxel j from a particular element and an X-ray intensity I_j is emitted from voxel j before entering voxel $j+1$, as defined in Fig. 5(b). The ratio I_j/I_0 can be obtained by integrating over the voxel, similarly as in Eq. (3). Since Δx is small, the integral is approximated by the function itself, $\int_0^{\Delta x} f(x)dx = f(\frac{\Delta x}{2})\Delta x$, and

$$\frac{I_j}{I_0}\approx\exp\left\{-\left(\frac{\mu}{\rho}\right)_j\rho_j\frac{\Delta x}{2}\right\} \quad (5)$$

The final intensity I, emitted from voxel $x^*=n_{max}$ at the surface of the sample, is calculated by applying to I_j the absorption correction factor obtained with Eq. (5), of each subsequent voxel $x^*=j+n$ encountered along the X-ray path:

$$\frac{I}{I_j}=\exp\left\{-\sum_{n=j+1}^{n_{max}}\left(\frac{\mu}{\rho}\right)_n\rho_n\Delta x\right\} \quad (6)$$

The absorption correction factor A_j^* is obtained by combining Eq. (5) and (6):

$$\frac{I}{I_0}=\frac{1}{A_j^*}=\exp\left\{-\left(\frac{\mu}{\rho}\right)_j\rho_j\frac{\Delta x}{2}-\sum_{n=j+1}^{n_{max}}\left(\frac{\mu}{\rho}\right)_n\rho_n\Delta x\right\} \quad (7)$$

The final absorption correction matrix A is obtained by calculating the factors A^* for all elements and all voxels x^*, y^* and z^*, and rotating them into the standard x, y, z reference frame.

In the acquired data, two detectors were used and the individual detector signals cannot be separated. If we assume that the detectors have the same efficiency and consider that the X-ray generation is isotropic, the correction matrix A for both detectors is approximated by the harmonic mean of the two absorption correction matrices calculated for each detector direction.

In Eq. (7), a value of density is needed for each voxel. With the ζ-factor method, the density can be obtained from the measured mass-thickness (Eq. (2b)). With the CL method, the density ρ_{el} can be estimated from the elemental fraction C_{el} with a weighted mean ($\rho=\sum C_{el}\rho_{el}$) or a harmonic mean ($1/\rho=\sum C_{el}/\rho_{el}$) or can be estimated from an external signal such as the HAADF-STEM tomogram. In this paper, the density is estimated from the weighted mean and from the HAADF signal.

As the absorption correction factors depend on the composition and vice versa, an iterative approach is required for both classical and 3D absorption correction. The general approach is the same: the iteration is initialised by calculating a composition C_0 with no absorption correction from the X-ray intensity I. In each iteration step, the absorption correction factors A_i are calculated from the composition C_i and applied to the X-ray intensity (I^*A_i) to obtain a new composition C_{i+1}.

For 3D absorption correction, the iterative process needs to include reconstruction and projection steps as shown in Fig. 6. The 3D matrix of elemental composition, $\mathbf{C}_0$, is first approximated without absorption correction: the tilt series of intensities, $\mathbf{I}_{\text{til},0}$, are reconstructed (rec) and the reconstructed intensities, $\mathbf{I}_{\text{vol},0}$, are quantified (quant). This first approximation $\mathbf{C}_0$ is used to calculate the absorption correction matrix, $\mathbf{A}_1$, for each tilt angle.

The reconstruction might introduce artefacts as absorption effects are likely to break the tomographic requirement. The

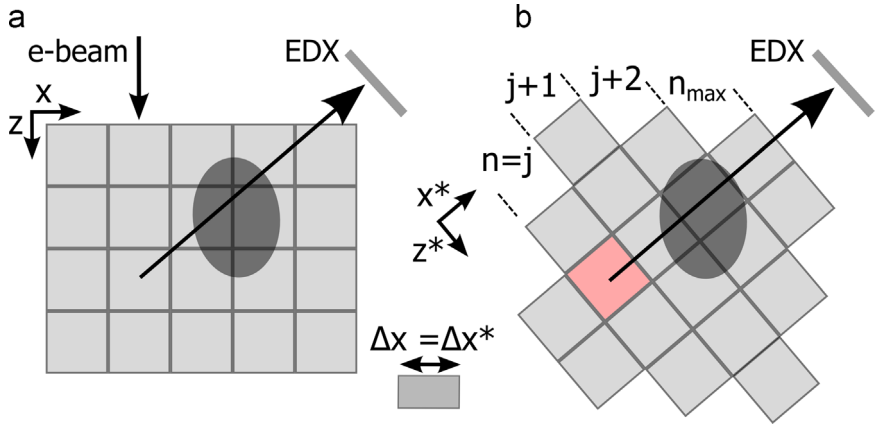

Fig. 5. Calculation of the absorption correction matrix, **A** from the matrix of elemental fraction $\mathbf{C}_{\text{vol}}$. The arrows indicate the path of the X-ray towards the detector. The array of square represent the voxel. The grey scale represents the elemental fraction of one element in the voxel. The same elemental map is represented in the two different referentials. In (a), the z axis is parallel to the electron beam. In (b), the x^* axis is parallel to the detector direction.

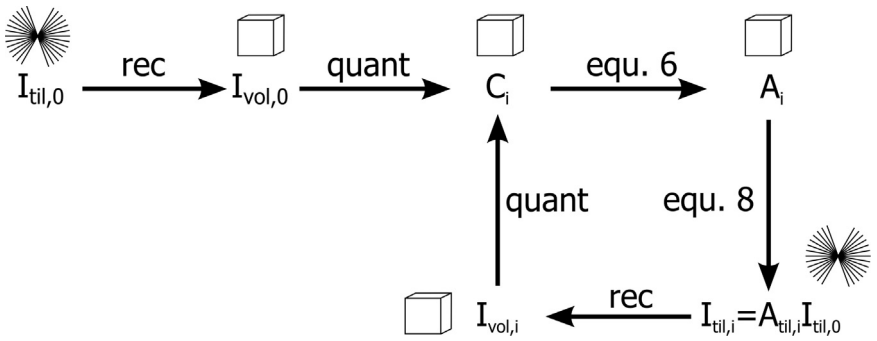

Fig. 6. Details of the iterative process for 3D absorption correction. Composition **C** are quantified (quant) from X-ray intensities **I** that are corrected by absorption correction factors **A**. The 3D intensities matrix $\mathbf{I}_{vol}$ are reconstructed (rec) from tilt series of intensities $\mathbf{I}_{til}$ at each i step of the iteration.

absorption correction matrix ($\mathbf{A}_1$) is thus applied to the tilt series of recorded intensities $\mathbf{I}_{til,0}$ and thus required to be projected about the tilt axis. A projection, sum along the beam direction, of $\mathbf{A}_1$ is not possible as the absorption correction is not a linear operation. A corrected $\mathbf{I}_{til,1}$ is projected instead and compared to the projected $\mathbf{I}_{vol,0}$ to obtain an absorption correction factor $\mathbf{A}_{til,1}$ for the tilt series:

$$\mathbf{A}_{til,i}=\frac{\left[\mathbf{I}_{vol,i}\right]_{til}}{\left[\mathbf{I}_{vol,0}\right]_{til}}=\frac{\left[\mathbf{I}_{vol,0}\mathbf{A}_i\right]_{til}}{\left[\mathbf{I}_{vol,0}\right]_{til}} \quad (8)$$

where i is the number of iterations and the square bracket indicates a direct projection. The matrix of intensities $\mathbf{I}_{vol,1}$, is reconstructed from $\mathbf{I}_{til,1}$, and equal to $\mathbf{I}_{til,0}\mathbf{A}_{til,1}$, and quantified to obtain a new $\mathbf{C}_1$ for the next step of the iteration. The loop is stopped when the result of an iteration is close to the previous iteration, typically less than 0.001 wt% difference.

4. Results

To prevent beam damage, the electron dose seen by the sample is limited by reducing the time spent per spectrum. The raw spectra are therefore noisy with a mean number of counts per channel less than one. An effective de-noising technique is needed, as illustrated in Fig. 7. The set of data contains millions of spectra characterising only a limited set of chemical phases. This is a favourable case for a multivariate statistical approach such as principal component analysis (PCA). Using PCA, the set of spectra is decomposed and then a model of the data is reconstructed leaving the components characteristic of noise [42]. Prior to the decomposition, the data were scaled to take into account Poisson statistics [43]. Masking regions with lower counts, the vacuum and the carbon film, improves the separation between the noise and the signal components. To prevent any mixing between X-ray maps of low and high energy due to covariance, PCA is applied separately on the low and high energy part of the data set, as indicated by the split spectrum of Fig. 7. By inspection of the scree plot and the noise content in the individual components, the first eight and four components were chosen to reconstruct the model for the low and high energy datasets, respectively. As seen in Fig. 7, the PCA-adjusted spectrum is relatively noise-free and the continuous background is well defined. The noise is significantly reduced in the raw intensity map for O Kα. The effect of PCA on the other raw intensity map can be observed in Fig. 1 of the supplementary material.

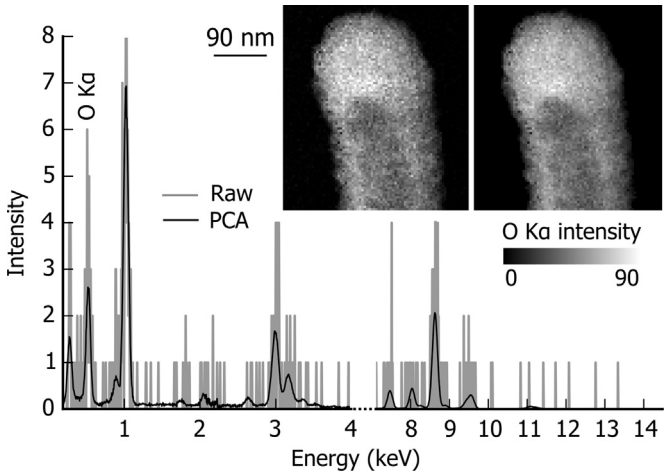

Fig. 7. Noise reduction using PCA. A spectrum is plotted before (grey) and after PCA decomposition/reconstruction (black). The spectrum is extracted from the data set at the position of an AgPt particle. The raw intensity map for O Kα (acquired at tilt 0°) is plotted before (left hand side) and after PCA decomposition/reconstruction (right hand side).

After noise filtering, the intensities are extracted and background corrected. Alignment of Ag Lα intensity maps is performed by automatic feature tracking and subsequently applied to the remaining elemental tilt series.

A general decrease of X-ray intensity due to shadowing is observed for maps close to 0° tilt, even when only the two EDX detectors facing the sample are employed. To correct for this effect, each X-ray elemental map is normalised [13].To prevent correcting the absorption effect when normalising, a X-ray line with low absorption (Zn Kα) was used to calculate the normalisation curve subsequently applied on each X-ray elemental map. The normalising curves for the different X-ray lines are plotted in Fig. 2 of the supplementary material. The main differences between the curve used for normalisation (Zn Kα) and the other curves are observed for X-rays emitted from small particles (Ag Lα and Au Lα) and for X-rays with low intensity.

The first 3D matrix of absorption correction factors $\mathbf{A}_1$ is obtained as described in the first line of Fig. 6. The reconstructed intensities are smoothed using a TV algorithm and the obtained intensities quantified using the CL quantification method. With this approach, the composition is normalised to 100% and voxels of vacuum and voids in the nanowire are filled with noise. Trial-and-error showed that all voxels in the composition matrix with a total X-ray intensity below 7 counts should be masked (30 counts are detected on average from voxels within the shell). $\mathbf{A}_1$ is obtained with Eq. (7) and the correction for O Kα is shown in Fig. 8. The detectors' direction goes in the direction of positive x and negative z with an angle of 22° with the x axis, as indicated by the "trail" in the vacuum in the xz section of Fig. 8. The correction is stronger in the direction opposite to that of the detectors. A linear structure is observed along the detectors' direction.

After the calculation of the first absorption correction matrix $\mathbf{A}_1$,

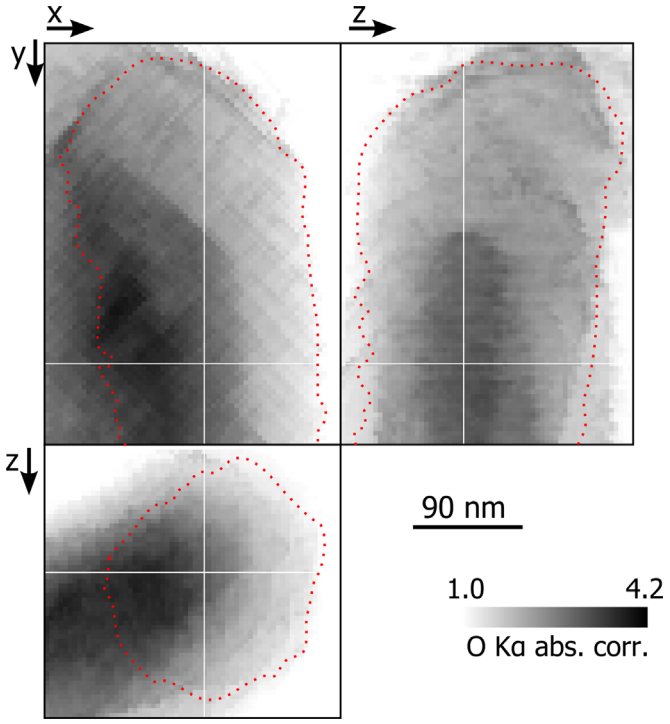

Fig. 8. Details of the 3D absorption correction factors. The maps give the absorption correction matrix $\mathbf{A}_1$, first iteration, for the O Kα intensity as orthogonal sections of the 3D volume. The white lines show the position of the orthogonal sections. The dashed line shows the limit outside which the total X-ray intensity is below 7 counts.

the tilt series are corrected as described in Eq. (8) and a new $\mathbf{A}_2$ is calculated. The effect of absorption correction after one and two iterations is considered in Fig. 9. In this figure, the grey scale gives the O Kα intensity of *x*-tilt sections, also known as a sinogram, through the tilt series ($\mathbf{I}_{\text{til}}$) for maps a, b and c, and through the corresponding projected reconstruction ($[\mathbf{I}_{\text{vol}}]_{\text{til}}$ as defined in Eq. (8) for maps d, e and f. The *x*-tilt section is positioned where the shell surrounds the core, as modelled by two circles in map g. Map h shows a projection of this model, which is only an approximation as the real shell shows a faceted aspect.

A jump in O Kα intensity is observed at zero tilt in Fig. 9(a) for the raw tilt series. This jump can be linked to an absorption effect: X-rays generated in the side of the shell opposite to the detectors travel further in the nanowire and are thus more likely to be absorbed. The jump reveals the change of detectors at 0° tilt (from detectors 3 and 4 to detectors 1 and 2, see Fig. 3). With the 3D absorption correction calculated after one iteration (map b), the intensity of the more absorbed side of the shell is increased: the jump in intensity is greatly reduced but can be still observed with an inverted contrast. With the absorption correction calculated after two iterations (map c), the jump is hardly noticeable.

As observed for all the projections (maps d, e, f and h), a corrected tilt series (one that conforms to the projection requirement) shows smoothly evolving contrast along the tilt direction. The jump observed in map a is thus an indication of that violation of the projection requirement. With reconstruction algorithms such as SART, the difference between the raw data $\mathbf{I}_{\text{til}}$ and the projected reconstruction $[\mathbf{I}_{\text{vol}}]_{\text{til}}$ is minimised during the reconstruction process, thanks to the so-called data fidelity constraint. In other words, maps d, e and f are the closest approximations to maps a, b and c, respectively. The jump in map a is approximated by a smoothly evolving contrast in map b, resulting in an important difference between map a and map b. After absorption correction, $\mathbf{I}_{\text{til}}$ and $[\mathbf{I}_{\text{vol}}]_{\text{til}}$ are more similar, indicating that a higher data fidelity is reached.

The iterative convergence of the absorption correction (see Fig. 6) is considered in more detail in Fig. 10. The convergence criterion, the root-mean-square (RMS) of the difference of the reconstruction corrected after i iterations and $i+1$ iterations, is plotted as a function of the number of iterations. In this logarithmic plot, a near-linear behaviour is observed after the first iteration for the different X-rays, indicating a fast convergence.

The reconstructed intensities of elements present in the shell of the nanowire are shown in Fig. 11: the shell is composed of zinc and oxygen. For both elements, the reconstructions obtained with or without absorption correction are compared. The corrected intensities of Zn Kα are not displayed as the absorption correction is small, with 95% of the voxels having an absorption correction below 0.8%

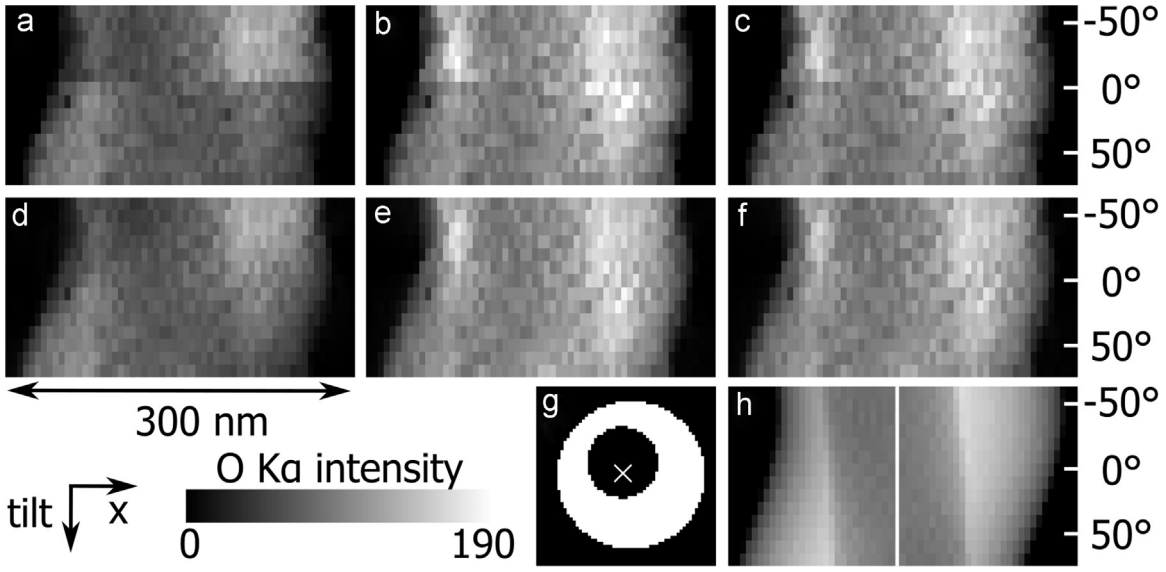

Fig. 9. 3D Absorption correction effect on tilt series after one and two iterations. The maps give the O Kα intensity as x-tilt sections: the tilt series ($\mathbf{I}_{\text{til}}$ for maps a, b and c) and the direct projection of $\mathbf{I}_{\text{vol}}$ ($[\mathbf{I}_{\text{vol}}]_{\text{til}}$ for maps d, e and f). Map a and d are not corrected for absorption. Map b and e are corrected after one iteration. Map c and f are corrected after two iterations. Map h is the direct projection of a model of the shell shown in map g (where *x* indicates the tilt axis).

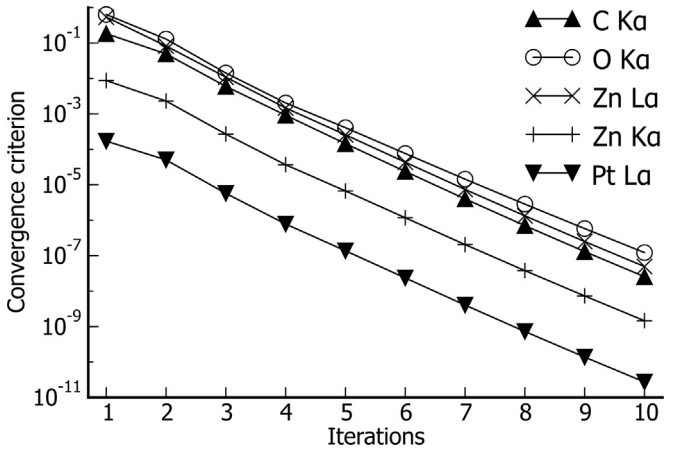

Fig. 10. Convergence of the iterative process for the 3D absorption correction calculation. The convergence criterion is the RMS difference of the reconstruction corrected after i iterations and $i+1$ iterations ($\mathbf{I}_i - \mathbf{I}_{i+1}$). The X-ray lines are sorted by increasing energy.

(compared to 32% for the Zn Lα intensity). The uncorrected intensities of the Zn Kα (map f) are thus used as an absorption-free reference. The effect of absorption can be observed comparing O Kα intensity (map a) with Zn Kα intensity (map f). In map a, the shell appears almost absent for low values of z in the zy section but appears more even in the xy section. A similar but less marked drop in intensity can be observed in map d for the Zn Lα intensity. The absorption effect is thus observed primarily along the z axis (optic axis), which is the resultant of all four detectors' directions. This drop in intensity is an artefact of the reconstruction algorithm due to the uncorrected X-ray maps not being true projections.

This reconstruction artefact is greatly reduced by applying the absorption correction; for example the Zn Lα intensity in map e of Fig. 11 appears to match closely the Zn Kα intensity in map c. The O Kα intensity in map b now looks similar to the Zn Kα intensity, but a slight over-correction is observed with high intensity at low value of z. For a more accurate comparison, a profile along the z axis going through the shell at the position indicated by the coloured lines in Fig. 11(a–f) is considered in Fig. 11(g). The intensities plotted are smoothed by a TV filter and normalised with the maximum of the profile in the right-hand part of the shell that shows less absorption effect. An absorption effect is clearly observed on the left-hand part of the shell for O Kα and Zn Lα intensities. After absorption correction, a close match is observed between Zn Lα and Zn Kα intensities. The O Kα intensity is closer to Zn Kα intensities, although slightly over-corrected. This can be attributed to the weighted mean approach used to estimate the density from the composition.

Given the relatively low mass-thickness of the nanowire, the intensity of HAADF-STEM images is assumed to be proportional to the mass-thickness. The density can be estimated by scaling the HAADF-STEM images to a region with a known density. Using the weighted mean approach, both core and shell have similar density but when using the HAADF-STEM approach, the density of the core is significantly lower that the density of the shell. With a shell expected to be composed of ZnO and the weighted mean density in the shell close to the density of the ZnO, this density is used to scale the HAADF-STEM images. The obtained density is used to calculate the absorption correction. By calculating the absorption correction with the HAADF-STEM density, a more accurate result is obtained as observed in the profile of Fig. 11(g) with the corrected O Kα intensity now closer to the Zn Kα intensities. It is worth noting that the density obtained with HAADF-STEM images introduces a different source of inaccuracies; for example a contrast variation in the shell due to diffraction. The weighted mean density is kept as a method of choice for a direct evaluation of the 3D absorption correction, as it does not require any a priori knowledge of the sample.

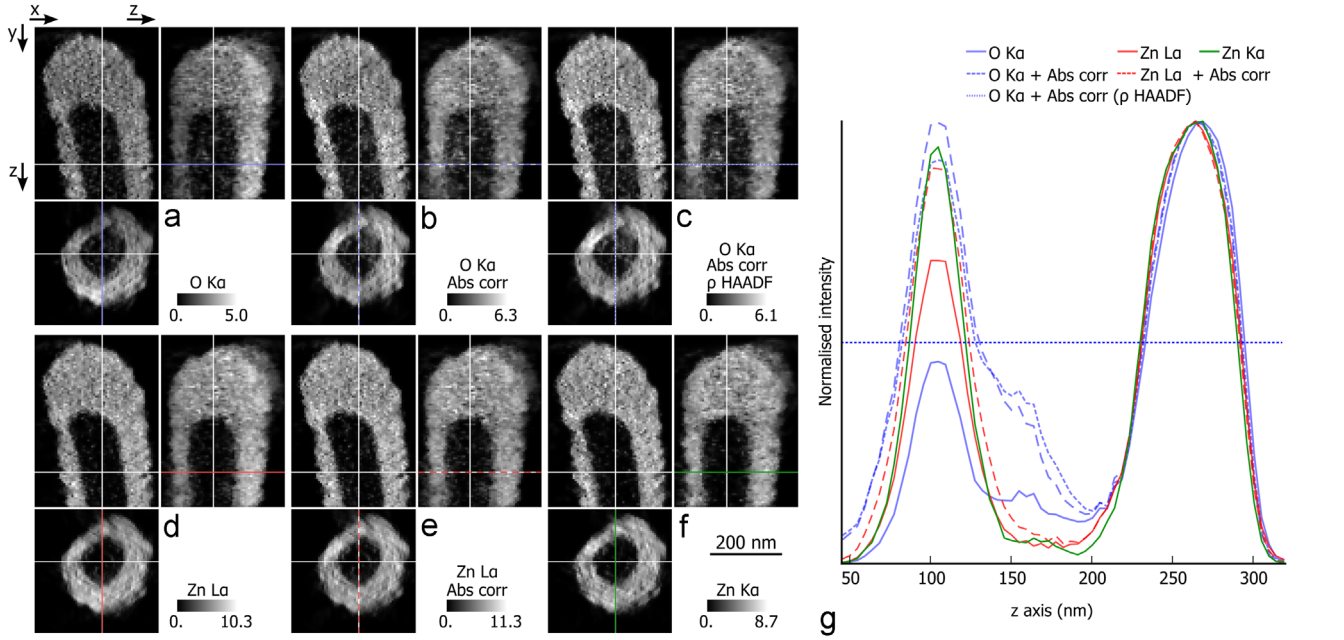

Fig. 11. Details of the reconstruction of the shell. Comparison of intensities without (maps a, d, f) and with (maps b, c, e) 3D absorption correction after 10 iterations. The density is estimated from a weighted mean (Abs corr) in maps b and e and from HAADF images (Abs corr ρ HAADF) in map c. The grey scale maps give the orthogonal sections of the reconstructed volume of the intensity of O Kα (maps a, b, c), Zn Lα (maps d, e) and Zn Kα (map f). The white lines show the position of the orthogonal sections. In (g), profiles along z are plotted for O Kα, Zn Lα and Zn Kα intensities. The position of profiles is indicated with coloured lines in the orthogonal sections. Intensities are normalised with the maximum of the profile in the right part of the shell that shows a smaller absorption effect. The horizontal dashed lines show the values used for the isosurfaces in Fig. 13. All intensities are smoothed by TV filter. (For interpretation of the references to colour in this figure legend, the reader is referred to the web version of this article.)

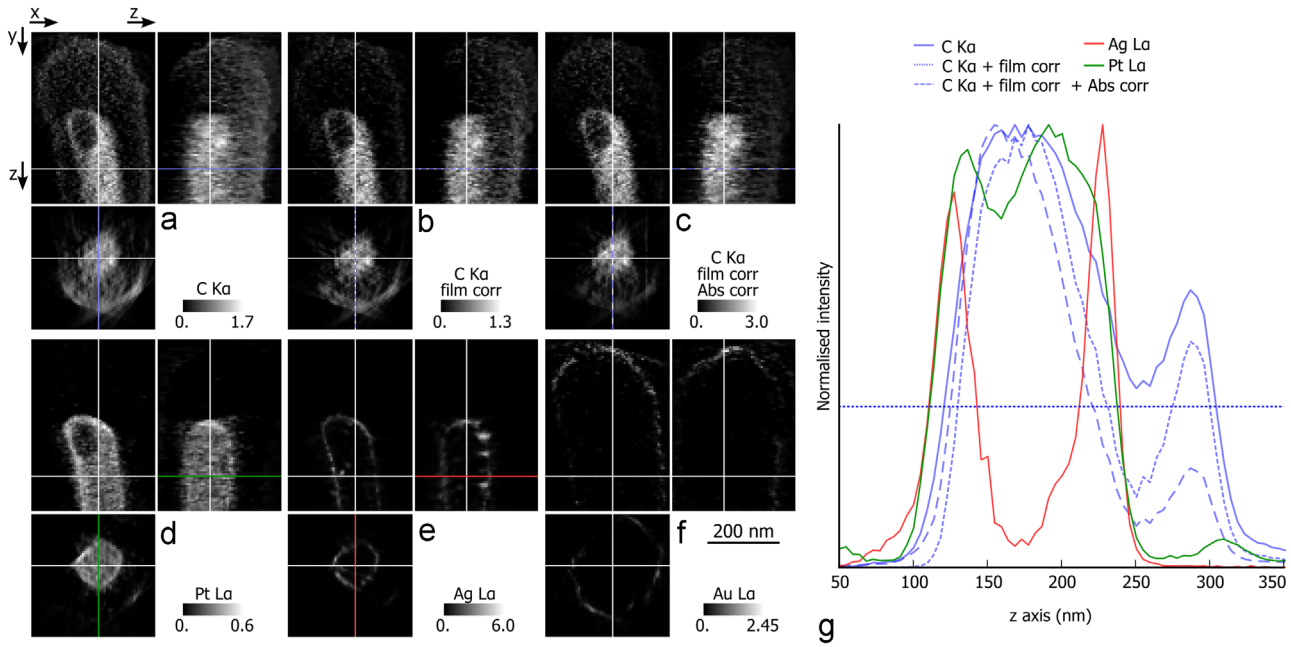

Fig. 12. Details of the reconstruction of the core. Comparison of intensities without (maps a, b, d, e) and with 3D absorption correction after 10 iterations ("Abs corr" in map c). The grey scale maps give the orthogonal sections of the reconstructed volume of the intensity of C Kα (maps a, b, c), Pt Lα (map d), Ag Lα (map e) and Au Lα (map f). Map b and c are corrected for the carbon supporting film (film corr). The white lines show the position of the orthogonal sections. In (f), profiles along *z* are plotted for C Kα, Pt Lα and Ag Lα intensities. The position of profiles is indicated with coloured lines in the orthogonal sections. Intensities are normalised with the maximum of the profile. The horizontal dashed lines show the values used for the isosurfaces in Fig. 13. All intensities are smoothed by TV filter. (For interpretation of the references to colour in this figure legend, the reader is referred to the web version of this article.)

The reconstructed intensities of the elements present in the core are shown in Fig. 12: the core is formed of a porous mixture of carbon and platinum and contains small particles composed of silver. Platinum and silver form a layer around the core and a layer of gold is observed on the tip of the nanowire in map f. A schematic picture of the sample is shown in Fig. 2(a). A larger void is observed at the tip of the core.

Reconstructions obtained with and without absorption correction are compared. The corrected intensities of Pt Lα and Ag Lα are not displayed as the absorption is small. The C Kα intensity has the highest value of absorption correction. In map a, the C Kα intensity is present in the shell with strong variation in contrast. As the supporting film is composed of carbon, a value of C Kα intensity emitted from the film is estimated for each tilt from regions that are known to be film only and removed from the tilt series before the reconstruction. In map b, the resulting C Kα intensity reconstruction is generally lower in the shell and the shape of the core observed in the *xz* section is better defined. In some regions with high *z* value, the intensity of the shell is however similar to the one in the core. After absorption correction, the C Kα intensity (map c) in the core is clearly above the intensity in the shell.

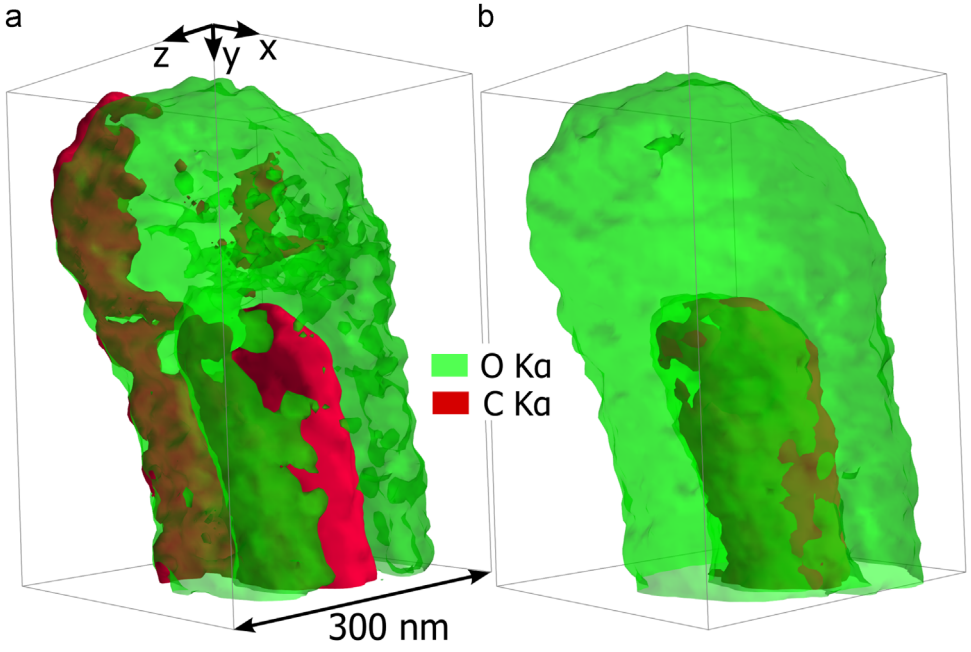

Fig. 13. Details of measured core and shell. The isosurfaces are reconstructed from the volume of O Kα and C Kα intensity with and without 3D absorption correction calculated after 10 iterations for figure (a) and (b), respectively. The thresholds used to generate the isosurfaces are indicated in Figs. 11(g) and 12(g) by a dashed blue line.

A profile along z through the core is plotted in Fig. 12 (g). As for the shell in Fig. 11, intensities are smoothed by a TV filter and normalised with the maximum of the profile. An important shoulder is observed for high values of z on the C Kα profile. The shoulder is significantly reduced, first by correcting for the supporting film, then by correcting for absorption. These processing steps contribute towards a more uniform C Kα intensity inside the core.

The absorption correction for the two strongest absorbing X-ray lines provides an important improvement that can be appreciated in 3D in Fig. 13. The green and red isosurfaces indicate a high O Kα and C Kα intensity respectively. The threshold values used are indicated by a horizontal dashed line in the z profiles of Figs. 11(g) and 12(e). The shell formed by the uncorrected O Kα intensity is not complete: a hole is observed for low values of z in Fig. 13(a). With a higher value of threshold, a complete shell can be obtained. The core formed by the uncorrected C Kα intensity shows an appendage towards high values of z. With higher values of threshold, the appendage is suppressed, but the void at the tip of the core is then not visible. Correcting for absorption in Fig. 13 (b), the shell is complete for any value of threshold and the void at the tip of the core can be observed without any appendage for an appreciable range of thresholds. The artefacts and their correction can be appreciated with more details in the supplementary animated figure (Appendix A) varying the view and the thresholds of the isosurfaces. The second video shows a reconstruction of X-ray lines from the different elements.

5. Discussion

Absorption introduces a contrast mechanism that breaks the "projection requirement" if not taken into account. The reconstruction algorithm finds the closest estimation that respects the requirement by introducing an artefact observed as a gradient of intensity in the unexpected direction of the electron beam. By applying the proposed 3D absorption correction, this artefact is almost totally removed in the case of the moderately absorbed Zn Lα intensity, as observed in Fig. 11(g) with a close match with Zn Kα intensity in term of shape. The Zn Kα intensity shows little absorption in the nanowire. Moreover, the risk of mixing Zn Lα and Zn Kα signals in the PCA de-noising process is prevented by applying PCA separately on low and high energy datasets, as proposed in [44]. The Zn Kα intensity is thus considered as an absorption-free reference for the Zn Lα intensity. The reference is relative as the cross-section of Zn Kα and Zn Lα is different, but as the part of the shell facing the detector emits X-rays with low absorption, an absolute reference can be deduced. As the shell is expected to be composed by a single phase of Zn and O and no experimental evidence shows the contrary, the Zn Kα intensity is also considered as an absorption-free reference for O Kα intensity.

Being more absorbed than the Zn Lα, the O Kα intensity requires a higher absorption correction and is thus more sensitive to inaccuracies. In Fig. 11, the absorption artefact is greatly reduced with a corrected O Kα intensity close to the Zn Kα intensity. The absorption correction is however sensitive to the method used to obtain the density. Deducing the density from the composition, porosities have to be differentiated from the material by using a mask, as compositions are normalised to 100%. This approach relies on the accuracy of masking porosities, which is limited for instance by sub-pixel voids. If we take the HAADF signal as proportional to the mass-thickness, the density of the porous core is directly estimated without masking. A lower density of the core is obtained with this approach, resulting in an improved absorption correction for O Kα intensity as observed in Fig. 11. However, the accuracy of this approach is limited by the need of a reference and by possible diffraction artefacts leading to variation in intensity. Moreover, an a priori knowledge of the sample is needed to scale the density.

The C Kα line is the most absorbed of the analysed X-rays and an important increase of C Kα intensity in the core is observed in Fig. 12 with the absorption correction. As the carbon is situated mainly in the core, all C Kα X-rays have an approximately similar path through the shell to reach the surface. The structure of the core formed by C Kα intensity is thus less affected by absorption than the shell formed by O Kα intensity. The accuracy of the absorption correction for this line is difficult to evaluate, having no reference for the carbon composition. The C Kα intensity emitted from the supporting film is observed to lower the quality of the core reconstruction in Fig. 12(a). A simple correction by intensity subtraction is shown to improve the core reconstruction. The accuracy of this approach is however limited by the high noise level of the C Kα intensity still present after PCA de-noising. The best way to prevent the problem of spurious X-rays from a supporting film is to use one free of elements present in the sample.

An important limitation of the EDX analysis is the low number of collected X-ray counts despite the high efficiency EDX system. In our case, the electron dose is limited to prevent significant beam damage and thus individual spectra have a low number of X-ray counts. The dataset is however formed of a high number of spectra measured on similar phases: a favourable case for statistical methods such as PCA. Using PCA to de-noise, each spectrum is significantly improved as shown in Fig. 7. As the background is significantly smoothed, the accuracy of the background correction by fitting is greatly improved.

The accuracy of the 3D absorption correction depends on the geometrical model of the microscope needed to approximate the path of the X-ray towards the detectors. In the proposed approach, a simple model is used: detectors are considered as points and the shadowing is assumed to be the same for each pair of detectors. With these assumptions, the absorption that takes place along the two paths is approximated by a mean absorption, calculated for each detector direction. To ascertain the accuracy of this approximation, the efficiency of each detector was experimentally measured at 0° tilt and very similar results were obtained. The accuracy of the absorption correction relies also on the elevation angle, a value not easily determined as it depends on the precise eucentric height and the sample holder used.

A more complex geometrical model could be used to improve the accuracy of the proposed approach for 3D absorption correction. As detectors are large and the detector-to-sample distance comparable, 30 mm^2 and 10.5 mm respectively, the take-off angle varies over the angular spread of the detector disc. With an appropriate weighted mean of the absorption correction matrix for the angular positions within the detector, a more accurate absorption correction matrix could be obtained. However, the accuracy of such an approach will be limited by the need for an accurate knowledge of the detector geometry and an accurate model of the detector shadowing.

For the absorption correction to be accurate, all X-ray intensities need to be accurately reconstructed. Reconstruction techniques, such as the SART algorithm used here, are known to suffer from artefacts when the tilt series has a low number of projections and/or a limited tilt range forming the so-called "missing wedge" [45]. Due to the low number of projections, the reconstructed intensity is correlated to the size of the object. This is observed with the reconstructed shell from the model in Fig. 9(g) and from the measured X-ray intensity in Fig. 11 (g): the smaller part of the shell has a lower intensity. Due to the missing wedge, other variations in contrast depending on the angular position are observed in the reconstructed model of the shell. These two artefacts are not expected to have a major influence on the accuracy of the absorption correction: the composition variation is limited as the composition is normalised to 100% and as the X-ray lines are expected to suffer proportionally with these artefacts. The composition of Zn in the large and small part of the shell are indeed observed to be much closer to that expected from the Zn Kα intensity.

Another artefact linked to the low number of projections is the loss of contrast between internal voids and the material: some remaining Zn Kα and O Kα intensity is observed in the core in Fig. 11(g), when the core is expected to be free of these elements. Albeit in small quantity, these misplaced intensities increase the calculated absorption of the core, contributing to the over-correction of O Kα intensity. A more recent reconstruction algorithm based on compressed sensing (CS) has proven to be more robust to low number of projections and the missing wedge [45]. The mentioned artefacts are expected to be reduced with CS, resulting in an improved absorption correction. Although not present in the case of a nanowire, there is another artefact that could have an important impact on the absorption correction: if the sample is slab-like, the reconstruction of the slab using emitted X-ray intensities is likely to suffer from truncation artefacts brought about by a change in the field of view as a function of tilt. The best way to prevent this is to use a needle sample extracted with a focused ion beam (FIB).

Finally, a major source of uncertainty for any EDX quantification procedure is the *k*-factors. The *k*-factors used here, provided by the manufacturer, are derived from first principle, an approach likely to suffer significant systematic error [46]. To reduce this error, *k*-factors should be experimentally determined, requiring standards with multiple elements of known composition and thickness. With the more recent ζ-factor quantification method, these constraints are reduced as single element standards or a universal thin film standard can be used. Such approach has shown to reduce significantly the systematic error [40]. Moreover, this method provides, alongside the measurement of the composition, a measurement of the mass-thickness, from which a density can be derived and used in the proposed 3D absorption correction. Such a density is expected to be more sensitive to porosity as it is obtained directly from the X-ray intensity with no normalisation, see Eq. (2b). This promising technique cannot however be used for the present dataset because of two unmet requirements: an accurate measurement of the current and a constant detector efficiency over the full tilt range are needed. A finer control of the detector shadowing is also required, for example by improving the acquisition using different grid geometries and sample holder, or by using a FIB-needle sample. Overcoming these experimental limitations is crucial for making EDX-STEM tomography fully quantitative and applicable to a wide range of nanomaterials.

6. Conclusions

A novel 3D absorption correction method is proposed for 3D EDX-STEM tomography. The assumptions of the classical absorption correction methods, constant X-ray generation and homogeneous absorption along the path to the surface, are refined by considering X-ray generation and absorption voxel by voxel. The approach is applied to three highly absorbed X-ray lines, Zn Lα, O Kα and C Kα, measured on a core/shell nanowire. The accuracy of the approach is assessed comparing X-ray lines with high absorption (Zn Lα, O Kα) to one with low absorption (Zn Kα). The absorption is the cause of an important artefact in the reconstruction, observed as X-ray intensity variation in the direction of the optic axis and resulting in a discrepancy of the shell and an appendage of the core. Applying the 3D absorption correction, this artefact is greatly reduced: the shell morphology formed by the O Kα intensity projection is near complete and the appendage of the core formed by the C Kα intensity projection is removed. Using the 3D absorption correction, 3D EDX-STEM tomography can be extended to highly absorbed X-ray lines with a greatly improved accuracy.

Acknowledgements

The research leading to these results has received funding from the European Union Seventh Framework Programme under Grant agreement 312483-ESTEEM2 (Integrated Infrastructure Initiative–I3), as well as from the European Research Council under the European Union's Seventh Framework Programme (FP/2007-2013)/ERC Grant agreement 291522-3DIMAGE. A.N.F. and A.B. acknowledge project MAT2013-42900-P from the Spanish Ministry of Economy and Competitiveness and REGPOT-CT-2011-285895-Al-NANOFUNC. Thanks to Francisco de la Peña for the fruitful discussion about PCA and Hyperspy [33].

Appendix A. Supplementary material

Supplementary data associated with this article can be found in the online version at http://dx.doi.org/10.1016/j.ultramic.2015.09.012.

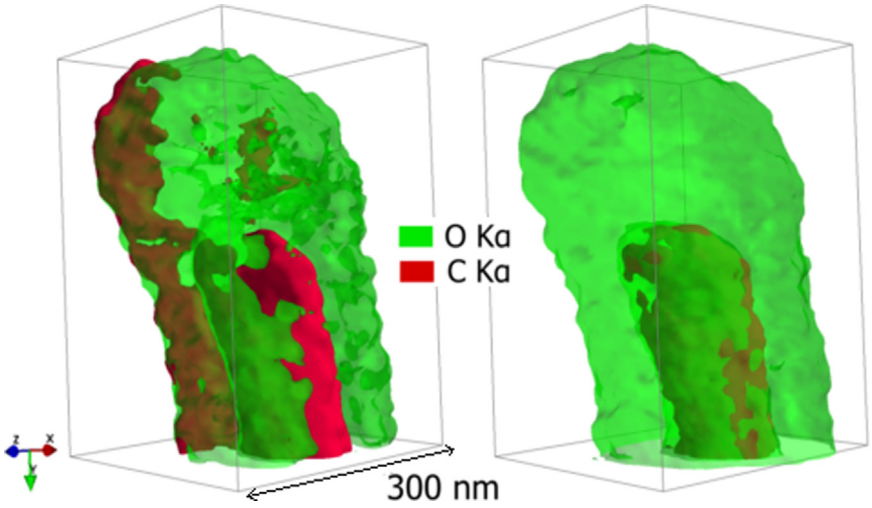

Movie 1. Details of the 3D measurements on the core/shell nanowire. This figure is an animated version of Fig. 13. The isosurfaces are reconstructed from the volume of O Kα and C Kα intensity. On the left side, the intensities are not corrected for absorption. On the right side, the intensities are corrected for absorption with the proposed 3D approach. The thresholds used to generate the isosurfaces vary from 50% to 150% of the values used in Fig. 13. A video clip is available online.Supplementary material related to this article can be found online at http://dx.doi.org/10.1016/j.ultramic.2015.09.012.

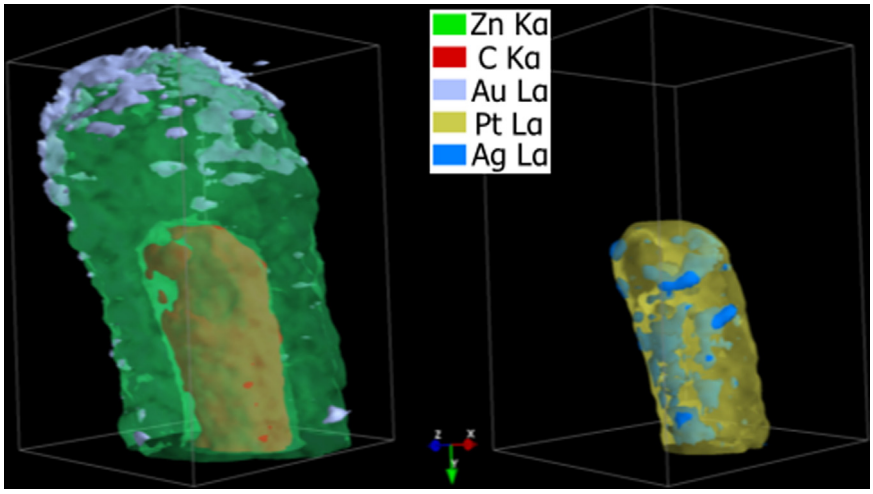

Movie 2. Details of the 3D measurements on the core/shell nanowire. The isosurfaces are reconstructed from the volume of the Zn Kα, C Kα and Au Lα intensities on the left-hand side and the Pt Lα and Ag Lα intensities on the right-hand side.A video clip is available online.Supplementary material related to this article can be found online at http://dx.doi.org/10.1016/j.ultramic.2015.09.012.

References

[1] J.I. Goldstein, Principles of thin film x-ray microanalysis, in: J.J. Hren, J. I. Goldstein, D.C. Joy (Eds.), Introduction to Analytical Electron Microscopy, Springer, US, 1979, pp. 83–120.

[2] S.J.B. Reed, Electron Microprobe Analysis, 2nd edition, Cambridge University Press, Cambridge, Uk, 1997.

[3] D.B. Williams, C.B. Carter, The Transmission Electron Microscope, Springer, US, 1996.

[4] M. Watanabe, X-ray energy-dispersive spectrometry, in: S.J. Pennycook, P. D. Nellist (Eds.), Scanning Transmission Electron Microscopy, Springer, New York, 2011, pp. 291–29351.

[5] P. Schlossmacher, D.O. Klenov, B. Freitag, S. von Harrach, A. Steinbach, Nanoscale chemical compositional analysis with an innovative S/TEM-EDX system, Microsc. Anal. 142 (2010) S5.

[6] L. Strueder, P. Lechner, P. Leutenegger, Silicon drift detector—the key to new experiments, Naturwissenschaften 85 (11) (1998) 539–543.

[7] H. Von Harrach, P. Dona, B. Freitag, H. Soltau, A. Niculae, M. Rohde, An integrated multiple silicon drift detector system for transmission electron microscopes, J. Phys.: Conf. Ser. 241 (2010).

[8] K. Lepinay, F. Lorut, R. Pantel, T. Epicier, Chemical 3D tomography of 28 nm high K metal gate transistor: STEM XEDS experimental method and results, Micron 47 (2013) 43–49.

[9] P. Burdet, J. Vannod, A. Hessler-Wyser, M. Rappaz, M. Cantoni, Three-dimensional chemical analysis of laser welded NiTi-stainless steel wires using a dual-beam FIB, Acta Mater. 61 (8) (2013) 3090–3098.

[10] A. Genc, L. Kovarik, M. Gu, H. Cheng, P. Plachinda, L. Pullan, B. Freitag, C. Wang, XEDS STEM tomography for 3D chemical characterization of nanoscale particles, Ultramicroscopy 131 (2013) 24–32.

[11] P. Burdet, C. Hébert, M. Cantoni, Enhanced quantification for 3D energy dispersive spectrometry: Going beyond the limitation of large volume of X-ray emission, Microsc. Microanal. 20 (5) (2014) 1544–1555.

[12] B. Goris, L. Polavarapu, S. Bals, G. Van Tendeloo, L. Liz-Marzan, Monitoring galvanic replacement through three-dimensional morphological and chemical mapping, Nano Lett. 14 (6) (2014) 3220–3226.

[13] C.S.M. Yeoh, D. Rossouw, Z. Saghi, P. Burdet, R.K. Leary, P.A. Midgley, The dark side of EDX tomography-modelling detector shadowing to aid 3d chemical signal analysis, Microsc. Microanal. 21 (3) (2015) 759–764.

[14] G. Haberfehlner, A. Orthacker, M. Albu, J. Li, G. Kothleitner, Nanoscale voxel spectroscopy by simultaneous EELS and EDS tomography, Nanoscale 6 (23) (2014) 14563–14569.

[15] T.J.A. Slater, A. Macedo, S.L.M. Schroeder, M.G. Burke, P. O'Brien, P.H. C. Camargo, S.J. Haigh, Correlating catalytic activity of Ag–Au nanoparticles with 3d compositional variations, Nano Lett. 14 (4) (2014) 1921–1926.

[16] G. Möbus, R. Doole, B. Inkson, Spectroscopic electron tomography, Ultramicroscopy 96 (3–4) (2003) 433–451.

[17] Z. Saghi, X. Xu, Y. Peng, B. Inkson, G. Möbus, Three-dimensional chemical analysis of tungsten probes by energy dispersive x-ray nanotomography, Appl. Phys. Lett. 91 (25) (2007).

[18] M. Schaffer, J. Wagner, B. Schaffer, M. Schmied, H. Mulders, Automated three-dimensional X-ray analysis using a dual-beam FIB, Ultramicroscopy 107 (8) (2007) 587–597.

[19] P. Midgley, M. Weyland, 3D electron microscopy in the physical sciences: the development of Z-contrast and EFTEM tomography, Ultramicroscopy 96 (3–4) (2003) 413–431.

[20] P. Midgley, R. Dunin-Borkowski, Electron tomography and holography in materials science, Nat. Mater. 8 (4) (2009) 271–280.

[21] R. Leary, Z. Saghi, M. Armbrüster, G. Wowsnick, R. Schlögl, J. Thomas, P. Midgley, Quantitative high angle annular dark-field scanning transmission electron microscope (HAADF-STEM) tomography and high resolution electron microscopy of unsupported intermetallic $GaPd_2$ catalysts, J. Phys. Chem. C 116 (24) (2012) 13343–13352.

[22] P. Hawkes, The electron microscope as a structure projector, Electron Tomography: Methods for Three-Dimensional Visualization of Structures in the Cell, Springer, US (2006), p. 83–111.

[23] J. Bullock, C. Humphreys, A. Mace, H. Bishop, J. Titchmarsh, Crystalline effects in the analysis of semiconductor materials using Auger electrons or X-rays, Inst. Phys. Conf. Ser. (76) (1985) 405–410 (Section 9).

[24] J.I. Goldstein, J. Costley, G. Lorimer, R.J.B. Reed, Quantitative X-ray analysis in the electron microscope, in: O. Johart (Ed.), Scanning Electron Microscopy, vol. 1, IITRI, Chicago IL, 1977, pp. 315–324.

[25] G. Cliff, G. Lorimer, The quantitative analysis of thin specimens, J. Microsc. 103 (2) (1975) 203–207.

[26] Z. Horita, K. Ichitani, T. Sano, M. Nemoto, Applicability of the differential X-ray absorption method to the determinations of foil thickness and local composition in the analytical electron micrscope, Philos. Mag. A 59 (5) (1989) 939–952.

[27] P.J. Statham, M.D. Ball, An indirect method for determining mass thickness for absorption corrections in the microanalysis of thin foils, in: D.B. Wittry (Ed.), Microbeam Analysis, San Francisco Press, San Francisco, CA, 1980, pp. 165–168.

[28] O. Eibl, New method for absorption correction in high-accuracy, quantitative EDX microanalysis in the TEM including low-energy X-ray lines, Ultramicroscopy 50 (2) (1993) 179–188.

[29] M. Watanabe, Z. Horita, M. Nemoto, Absorption correction and thickness determination using the ζ factor in quantitative X-ray microanalysis, Ultramicroscopy 65 (3–4) (1996) 187–198.

[30] M. Macias-Montero, A.N. Filippin, Z. Saghi, F.J. Aparicio, A. Barranco, J. P. Espinos, F. Frutos, A.R. Gonzalez-Elipe, A. Borras, Vertically aligned hybrid core/shell semiconductor nanowires for photonics applications, Adv. Funct. Mater. 23 (48) (2013) 5981–5989.

[31] Z.L. Wang, From nanogenerators to piezotronics—a decade-long study of ZnO nanostructures, MRS Bull. 37 (2012) 814–827.

[32] M. Alcaire, J.R. Sanchez-Valencia, F.J. Aparicio, Z. Saghi, J.C. Gonzalez-Gonzalez, A. Barranco, Y.O. Zian, A.R. Gonzalez-Elipe, P.A. Midgley, J.P. Espinos, P. Groening, A. Borras, Soft plasma processing of organic nanowires: a route for the fabrication of 1D organic heterostructures and the template synthesis of inorganic 1D nanostructures, Nanoscale 3 (2011) 4554–4559.

[33] F. de la Peña, P. Burdet, T. Ostasevicius., M. Sarahan, M. Nord, V.T. Fauske, J. Taillon, A. Eljarrat, S. Mazzucco, G. Donval, L.F. Zagonel, M. Walls, I. Iyengar, Hyperspy: HyperSpy 0.8.1 (2015), http://dx.doi.org/10.5281/zenodo.27735.

[34] E.R. Malinowski, Factor Analysis in Chemistry, 3rd Edition, John Wiley & Sons Inc., 2002.

[35] D. Rossouw, P. Burdet, F. de laPeña, C. Ducati, B.R. Knappett, A.E.H. Wheatley, P. A. Midgley, Multicomponent signal unmixing from nanoheterostructures: overcoming the traditional challenges of nanoscale x-ray analysis via machine learning, Nano Lett. 15 (4) (2015) 2716–2720.

[36] C.O. Sorzano, C. Messaoudi, M. Eibauer, J.R. Bilbao-Castro, R. Hegerl, S. Nickell, S. Marco, J.M. Carazo, Marker-free image registration of electron tomography tilt-series, BMC Bioinform. 10 (1) (2009) 124.

[37] A.H. Andersen, A.C. Kak, Simultaneous algebraic reconstruction technique (SART): a superior implementation of the ART algorithm, Ultrason. Imaging 6 (1) (1984) 81–94.

[38] P. Ramachandran, G. Varoquaux, Mayavi: 3D visualization of scientific data,

Comput. Sci. Eng. 13 (2) (2011) 40–51.
[39] A. Chambolle, An algorithm for total variation minimization and applications, J. Math. Imaging Vis. 20 (1–2) (2004) 89–97.
[40] M. Watanabe, D.B. Williams, The quantitative analysis of thin specimens: a review 27 of progress from the Cliff–Lorimer to the new ζ-factor methods, J. Microsc. 221 (2) (2006) 89–109.
[41] J. Philibert, A method for calculating the absorption correction in electron-probe microanalysis, in: H.H. Pattee, V.E. Cosslett, A. Engström (Eds.), Proceedings Proceedings of the 3rd International Congress on X-Ray Optics and Microanalysis, Academic Press, New York NY, 1963.
[42] G. Lucas, P. Burdet, M. Cantoni, C. Hébert, Multivariate statistical analysis as a tool for the segmentation of 3D spectral data, Micron 52–53 (2013) 49–56.
[43] M. Keenan, P. Kotula, Accounting for Poisson noise in the multivariate analysis of ToF-SIMS spectrum images, Surf. Interface Anal. 36 (3) (2004) 203–212.
[44] P. Burdet, S. Croxall, P. Midgley, Enhanced quantification for 3D SEM-EDS: using the full set of available X-ray lines, Ultramicroscopy 148 (2015) 158–167.
[45] Z. Saghi, D. Holland, R. Leary, A. Falqui, G. Bertoni, A. Sederman, L. Gladden, P. Midgley, Three-dimensional morphology of iron oxide nanoparticles with reactive concave surfaces. A compressed sensing-electron tomography (CS-ET) approach, Nano Lett. 11 (11) (2011) 4666–4673.
[46] D. Newbury, D.B. Williams, J.I. Goldstein, C. Fiori, Observation on the calculation of kAB factors for analytical electron microscopy, in: D.B. Williams, D. C. Joy (Eds.), Analytical Electron Microscopy, San Francisco Press, San Francisco CA, 1984, pp. 276–278.